On the Stability of Balanced Rigid Rotors in Air Foil Bearings

Christoph Baum [1], **Hartmut Hetzler** [2], **Wolfgang Seemann** [1]

[1] Institute of Engineering Mechanics (ITM), Karlsruhe Institute of Technology (KIT), Kaiserstr. 10, 76131 Karlsruhe, Germany, {christoph.baum, wolfgang.seemann}@kit.edu
[2] Institute of Mechanics (IFM), University Kassel, Moenchebergstr. 7, 34125 Kassel, Germany, hetzler@uni-kassel.de

Abstract

A rigid rotor model and a reduced model of air foil bearings are introduced, coupled and solved simultaneously. The rotor and bearing structure models are kept simple, while the fluid model is reduced, aiming for time efficient numerical simulations to investigate fundamental physics, mainly the influence of bearing compliancy on the rotor dynamics. A run up simulation is performed to show the onset of whirl motion. Angular velocity depending stationary rotor positions and their stability are determined for a variation of the bearing compliance and the nondimensional rotor mass parameter. The topology of solutions is investigated by a bifurcation analysis, using numerical path following methods.

1 Introduction

Oil-free bearing concepts are a promising approach for optimising high speed rotating - and turbomachinery. Major advantages of air lubricated bearing systems, in comparison to oil lubricated bearing systems are power loss reduction, less maintenance costs, higher temperature resistance and higher operating shaft speeds, [4], [7]. As an improvement of self-acting (rigid) journal bearings, foil bearings were evolved to minimize instability problems, reduce manufacturing tolerances, and permit adaptation of the bearing to changes in shaft diameter caused by centrifugal force or temperature gradients, [6]. However, a crucial criterion for the choice of the bearing concept is the dynamical behavior of the rotor during operation, which is significantly influenced by the bearings. In particular, the bearing forces could lead to self excited vibrations. Consequently, disruptive rotor vibrations could occur, whereas a safe operation might not be possible. To this end, comprehensive knowledge of bearing characteristics and the interaction between bearings and rotor should be recognized to design an appropriate rotor bearing system.

In order to get more insights of the influences of air foil bearings, in particular the compliancy of the bearing, on the dynamical behavior of rotors, a coupled air foil bearing rotor model is investigated. The rotor and bearing model are kept simple, while the focus of this work is to understand the crucial physics of whirl instabilities and tendencies to influence their occurrence.

2 Rotor Model

The investigated rotor model is chosen as simple as possible, to solely study the effects of the air bearings on the dynamics of the rotor, without any excitation. Thus, a rigid rotor of mass $2M$ without static and dynamic unbalance, horizontally and symmetrically mounted by two identical bearings is assumed, see Figure 1. Due to the symmetry the investigated problem will be restricted to plane motions, whereas P states the center of the rotor, which coincides with the center of mass.

In order to describe the kinematics, a spaced fixed frame $\mathrm{I}(O, \boldsymbol{e}_x^\mathrm{I}, \boldsymbol{e}_y^\mathrm{I}, \boldsymbol{e}_z^\mathrm{I})$ and a co-rotation frame $\mathrm{II}(O, \boldsymbol{e}_r^\mathrm{II}, \boldsymbol{e}_\gamma^\mathrm{II}, \boldsymbol{e}_z^\mathrm{II})$ where $\boldsymbol{e}_z^\mathrm{I} = \boldsymbol{e}_z^\mathrm{II}$ are introduced, cf. Figure 1(b). The origin O of both frames is located on the connecting line between the center points of the bearings, while the axis of rotation is collinear to the $\boldsymbol{e}_z^\mathrm{I/II}$ axes. The angular velocity of the rotor $\boldsymbol{\omega} = \omega \boldsymbol{e}_z^\mathrm{I}$ is considered to be given and consequently is no degree of freedom. The orientation of the co-rotating frame II with respect to frame I is given by the angle γ. The position of P with respect to O is given by the Cartesian coordinates x_p and y_P with respect to system I. Likewise the position of P can also be defined by the eccentricity vector $\boldsymbol{e}_P = e_P \boldsymbol{e}_r^\mathrm{II}$, using polar coordinates e_P (eccentricity) and γ (attitude angle).
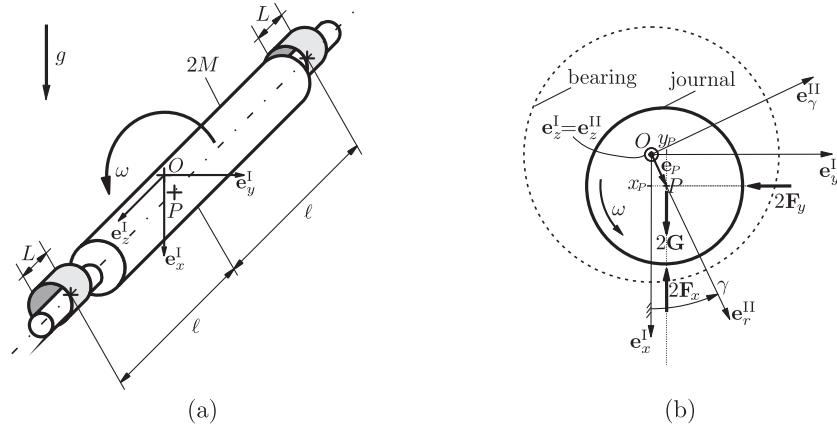
Figure 1: Model rotor in symmetrical bearings (a), free body diagram of rotor (b)

The conversion between these two descriptions are given by

$$e_P = \sqrt{x_P^2 + y_P^2} \quad , \qquad \tan\gamma = \frac{y_P}{x_P}. \tag{1}$$

Thus, the investigated rotor model has two degrees of freedom, either x_P, y_P or e_P, γ.

Applying the forces given in the free body diagram (Figure 1(b)), Newton's 2nd law yields the equations of motion

$$M\ddot{x}_P + F_x = Mg \tag{2}$$
$$M\ddot{y}_P + F_y = 0 \tag{3}$$

where F_x, F_y are the components of the bearing force of either bearing in e_x^I- and e_y^I-direction, which are nonlinear functions depending on the state of the journal and its angular velocity.

$$F_i = F_i(x_P, y_P, \dot{x}_P, \dot{y}_P, \omega), \quad i = x, y. \tag{4}$$

3 Bearing Model

Figure 2(a) shows a sketch of the bearing with the relevant geometry parameters and coordinates. The nominal radius of the undeformed bearing is R, L is the bearing length, and r the journal's radius. The radial clearance of the undeformed bearing is $h_0 = R - r$. The fluid film height is given by $h - q$, while h states the variation due to the displacement of the rotor with respect to the undeformed bearing wall and q the wall deflection. Both, h and q are functions of the circumferential coordinate φ, starting at the spatially fixed e_x^I-axis, and an axial coordinate. Since the maximum eccentricity $e_{P,\max}$ for air bearings is typically small compared to the geometry parameters of the bearing ($e_{P,\max} \gg R, r, L$), the gap height h with respect to the undeflected bearing wall can be expressed as
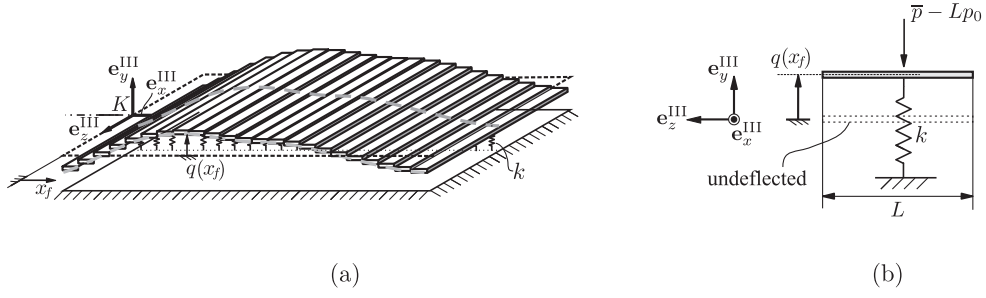
$$h \approx h_0 - e_P \cos(\varphi - \gamma), \tag{5}$$

assuming the co-centricity of journal axis and symmetry axis of the bearing. Using addition theorems, the gap height (5) can be expressed in terms of the Cartesian coordinates

$$h \approx h_0 - x_P \cos(\varphi) - y_P \sin(\varphi). \tag{6}$$

Furthermore, by considering a small fluid height $h - q$ compared to its length in circumferential direction, the curvature of the fluid film can be neglected, cf. [13] f.i.. Consequently a plane description of the fluid film area using Cartesian coordinates may be used, where $x_f = R\varphi$ is the circumferential and z_f is the axial position (see Figure 2(b)).

Figure 2: Bearing geometry and coordinates (a), unwrapped fluid plane and coordinates (b)

3.1 Fluid Modelling

Applying the common assumptions of fluid film lubrication theory [7], and assuming the fluid behaving as an ideal gas, the gas pressure p may be described by the Reynolds equation for compressible fluids (cf. [13] for instance)

$$\frac{\partial}{\partial x_f}\left[\frac{p(h-q)^3}{\mu}\frac{\partial p}{\partial x_f}\right] + \frac{\partial}{\partial z_f}\left[\frac{p(h-q)^3}{\mu}\frac{\partial p}{\partial z_f}\right] - 6\omega R\frac{\partial}{\partial x_f}\left[p(h-q)\right] - 12\frac{\partial}{\partial t}\left[p(h-q)\right] = 0. \tag{7}$$

in $\Omega_D = \{(x_f, z_f) \,|\, x_f = 0..2\pi R, z_f = -L/2..L/2\}$, where μ is the viscosity of the fluid, respective air. This partial differential equation is accompanied by the boundary conditions

$$p(z_f = -\frac{L}{2}) = p(z_f = \frac{L}{2}) = p_0, \quad , \quad p(x_f = 0) = p(x_f = 2\pi R) \tag{8}$$

see Figure 2(b) and the initial condition $p(x_f, z_f, t = 0) = p_{t_0}$. Once the pressure distribution has been determined from (7) with (8) and I.C., the bearing forces acting on the rotor can be determined by

$$F_x = \int_0^{2\pi}\int_{-\frac{L}{2}}^{\frac{L}{2}} p\cos(\varphi)\,\mathrm{d}z_f\,R\mathrm{d}\varphi \quad , \quad F_y = \int_0^{2\pi}\int_{-\frac{L}{2}}^{\frac{L}{2}} p\sin(\varphi)\,\mathrm{d}z_f\,R\mathrm{d}\varphi. \tag{9}$$

3.2 Structure Modelling

The compliant structure underneath the fluid film is model as massless, rigid elements with one finite dimension in axial (e_z^{III}) direction, supported by linear elastic springs (stiffness k), without any couplings in circumferential (e_x^{III}) direction, see Figure 3(a) and (b) respectively. This model is a further reduction of a 1D model presented and validated by San Andres and Kim in [12], neglecting the bending stiffness of the top foil in circumferential direction and the finite gap between the contact points of the foil and elastic support (bumps). On the other hand, the presented model has a slight enhancement compared to the simple elastic foundation model (Winklerfoundation) presented by Heshmat in [8], with the major advantage that eccentricities $e_P > 1$ are physically possible, since a deflection of the structure at the axial ends ($z_f = \pm\frac{L}{2}$), where the fluid pressure is equal the ambient pressure, see 8, is feasible. The deflection of a single axial element is given by

$$kq = -(\overline{p} - Lp_0), \tag{10}$$

where p_0 is the ambient pressure and

$$\overline{p} = \int_{-\frac{L}{2}}^{\frac{L}{2}} p\,\mathrm{d}z_f \tag{11}$$

Figure 3: 3D view of structure model (a), single rigid element of bearing structure (b)

the axial averaged pressure.

4 Nondimensional Equations
4.1 Fluid and Structure

Using the transformations

$$\varphi = \frac{x_f}{R}, \quad z_f^* = \frac{z_f}{L}, \quad \varepsilon_P = \frac{e_P}{h_0}, \quad x_P^* = \frac{x_P}{h_0}, \quad y_P^* = \frac{y_P}{h_0}, \quad p^* = \frac{p}{p_0}, \quad \tau = t\Omega, \tag{12}$$

for the independent and dependent variables, the fluid film height, the deflection of the structure and the angular velocity of the rotor are consequently transformed by

$$h^* = \frac{h}{h_0}, \quad q^* = \frac{q}{h_0}, \quad \omega^* = \frac{\omega}{\Omega}. \tag{13}$$

Substituting (12) and (13) in (7) leads to

$$\frac{\partial}{\partial \varphi}\left[p^*(h^* - q^*)^3 \frac{\partial p^*}{\partial \varphi}\right] + \kappa^2 \frac{\partial}{\partial z_f^*}\left[p^*(h^* - q^*)^3 \frac{\partial p^*}{\partial z_f^*}\right] - \omega^* \frac{\partial}{\partial \varphi}\left[p^*(h^* - q^*)\right] - 2\frac{\partial}{\partial \tau}\left[p^*(h^* - q^*)\right] = 0, \tag{14}$$

on $\Omega_{D^*} = \left\{(\varphi, z_f^*) \mid \varphi = 0..2\pi, z_f^* = -1/2..1/2\right\}$, with two geometric similarity parameters ψ, κ and the characteristic angular velocity and inverse time scale Ω

$$\psi = \frac{h_0}{R} \quad , \qquad \kappa = \frac{R}{L} \quad , \qquad \Omega = \frac{p_0 \psi^2}{6\mu} = \frac{p_0 h_0^2}{6\mu R^2}. \tag{15}$$

The scaled gap function h^* (5), (6) results as

$$h^* = 1 - \varepsilon_P \cos(\varphi - \gamma) = 1 - x_P^* \cos(\varphi) - y_P^* \sin(\varphi). \tag{16}$$

Applying the transformations (12) to the averaged pressure (11) leads to

$$\overline{p}^* = \frac{\overline{p}}{L\,p_0}, \quad \text{with} \quad \overline{p}^* = \int_{-\frac{1}{2}}^{\frac{1}{2}} p^*\, dz^*, \tag{17}$$

while the nondimensional structure equation (10) is given by

$$q^* = \alpha(1 - \overline{p}^*) \tag{18}$$

with the definition of a compliance parameter α as

$$\alpha = \frac{p_0 L}{k h_0} = \frac{p_0}{k \psi \kappa}. \tag{19}$$

A rigid bearing model is obtained for $\alpha = 0$.

4.2 Rotor

Using the transformations in (12), the rotor's equations of motion (2), (3) are reformulated as

$$x_P^{*''} + \Gamma F_x^* = \Xi \tag{20}$$

$$y_P^{*''} + \Gamma F_y^* = 0, \tag{21}$$

where a prime $(.)' = \frac{\mathrm{d}}{\mathrm{d}\tau}(.)$ denotes the derivate with respect to the nondimensional time τ. In (20) and (21), two additional nondimensional parameters

$$\Gamma = \frac{p_0 R L}{M h_0 \Omega^2}, = \frac{36 \mu^2 R^5 L}{p_0 M h_0^5}, \quad \Xi = \frac{g}{h_0 \Omega^2}, = \frac{36 g \mu^2 R^4}{p_0^2 h_0^5}, \tag{22}$$

are introduced. The parameter Γ is a characteristic force ratio of bearing and inertia force and Ξ is a characteristic force ratio of load and inertia force.

5 Model Dimension Reduction

With the objective of deriving a fast coupled nonlinear rotor bearing model, the dimension of the fluid equation (14) is reduced by using a Galerkin-approach of Kantorovich type [9] analog to [1]. Motivated by full numerical solutions using FD discretisation the unknown pressure function $p^*(\varphi, z_f^*, \tau)$ is assumed as a product

$$p_a^*(\varphi, z_f^*, \tau) = \sum_{i=1}^{n} \tilde{p}_{ai}^*(z_f^*) \hat{p}_{ai}^*(\varphi, \tau) + 1, \tag{23}$$

of time-invariant axial shape functions $\tilde{p}_{ai}^*$ only depending on the axial coordinate z_f^* and circumferential functions $\hat{p}_{ai}^*$, which depend on the nondimensional time τ and the circumferential coordinate φ. Here, the index a indicates that an approximation $p^* \approx p_a^*$ is determined. Assuming a one term parabolic axial shape function, the approximated solution takes the form

$$p_a^*(\varphi, z_f^*, \tau) = (\frac{1}{4} - z_f^{*2}) \hat{p}_{a1}^*(\varphi, \tau) + 1. \tag{24}$$

The approximated averaged pressure (17) for the assumed pressure function (24) is given by

$$\overline{p}_{a1}^* = \frac{1}{6} \hat{p}_{a1}^*(\varphi, \tau) + 1. \tag{25}$$

Substituting (18) in (14) and furthermore (24) and (25) into the resulting Reynolds equation, while demanding that the averaged weighted residuum vanishes eventually yields – after evaluation of integrals and appropriate rearranging – a reduced PDE and B.C. of the form

$$\frac{\partial \hat{p}_{a1}^*}{\partial \tau} = \hat{p}_{a1}^{*'} = f \left(\hat{p}_{a1}^*, \frac{\partial}{\partial \varphi} \hat{p}_{a1}^*, \frac{\partial^2}{\partial \varphi^2} \hat{p}_{a1}^*, x_P^*, y_P^*, x_P^{*'}, y_P^{*'}, \omega^*, \kappa, \alpha \right) \tag{26}$$

$$B.C.: \quad \hat{p}_{a1}^*(\varphi = 0) \overset{!}{=} \hat{p}_{a1}^*(\varphi = 2\pi) \quad \forall t, \tag{27}$$

on $\Omega_{D^* \text{red}} = \{(\varphi) \mid \varphi = 0..2\pi\}$.

Table 1: Parameter values

Non-dim. par.	Definition	Value	Non-dim. par.	Definition	Value
ψ	$\frac{h_0}{R}$	10^{-3}	Γ	$\frac{36\mu^2 R^5 L}{p_0 M h_0^5}$	0.5, 0.75, 1, 2, 4
κ	$\frac{R}{L}$	$\frac{1}{2}$	Ξ	$\frac{36 g \mu^2 R^4}{p_0^2 h_0^5}$	0.572
α	$\frac{p_0}{k\,\psi\,\kappa}$	0..2			

6 Discretisation and Parameters

For numerical approximations of (26), finite central differences (FD) of derivatives with respect to the remaining spatial coordinate φ

$$\frac{\partial}{\partial \varphi}\hat{p}_{a1}^* \approx \frac{\hat{p}_{j+1}^* - \hat{p}_{j-1}^*}{2\Delta\varphi} \quad , \quad \frac{\partial^2}{\partial \varphi^2}\hat{p}_{a1}^* \approx \frac{\hat{p}_{j+1}^* - 2\hat{p}_j^* + \hat{p}_{j-1}^*}{\Delta\varphi^2}. \tag{28}$$

are used. Thus, the reduced domain is divided into a uniform grid of m collocation points $\hat{p}_i^*, i = 1..m$. Together with the mechanical state variables of the rotor center P, a state-space-matrix

$$\boldsymbol{x} = [x_P^*, y_P^*, x_P^{*'}, y_P^{*'} \mid \hat{p}_1^*, \ldots, \hat{p}_j^* \ldots, \hat{p}_m^*]^T \tag{29}$$

of length $m + 4$ is defined. Using the state-space-matrix $\boldsymbol{x}$, a coupled first order system of nonlinear ODE can be defined

$$\boldsymbol{x}' = \boldsymbol{X}(\boldsymbol{x}(\tau)), \tag{30}$$

including the rotor equations (20) and (21) and the discretised fluid equations (26). The physical model presented here is quite similar to the model presented in [2] by Bonello and Pham, whereas the (linear) damping characteristic of the structure, as well as the static unbalance and accordingly the excitation is additionally neglected. In their contribution, the nonlinear fluid equation is also reduced by a Galerkin-approach. But in [2] Bonello and Pham are using different and more trial functions in axial direction, and furthermore trial functions in circumferential direction, too.

The system (30) is autonomous, since no explicit time dependence (e.g. harmonic excitation by unbalance) is existing. Time-integration of (30) is solved efficiently by means of standard solvers for initial value ODE-problems, using Matlab. The subsequent bifurcation analysis is conducted, using the continuation toolbox MatCont, [5]. For the following investigations the ambient pressure is chosen as $p_0 = 10^5$ [N m^{-2}], the viscosity of air as $\mu = 1.8 \cdot 10^{-5}$ [N s m^{-2}]. The values of the nondimensional parameters are listed in Table 1. Based on the chosen parameters, the time and angular velocity scale (15) can quantitatively be determined as $\Omega = 9.26 \cdot 10^2$ [s^{-1}].

7 Numerical Analysis - Results

7.1 Time Integration - Run Up

To show the applicability as well as the numerical efficiency of the presented model a run up simulation of the rotor is performed. Thus, the rotor speed is linearly increased between $n_{\text{low}} = 5000$rpm ($\omega^* = 0.57$) and $n_{\text{high}} = 12500$rpm ($\omega^* = 1.41$), within an interval of 30s. Figure 4, shows exemplarily some results of the state variables x_P^*, y_P^* of the rotor's center P, for the parameters $\alpha = 0.5, \Gamma = 2$. The simulation time, performed on an i5 CPU with 4GB ram was 350s. It is observable, that P remains at an almost fixed position ($\varepsilon_P' \approx \gamma' \approx 0$) at low speeds. After passing a certain threshold ω_s^*, self excited vibrations occur and the rotor starts to whirl with fast increasing radii and approximately half the angular velocity of the rotor ($\gamma' \approx \frac{\omega^*}{2}$), see Figure 4 (b), (c).

Motivating a bifurcation analysis, run down simulations with the same parameters and within the same time interval, solely switching start - and end rotor speed are performed. The state variables of the rotor are shown in Figure 4 (d). One obviously observes the difference in rotor speed or time interval, where the self excited vibrations during run up occur and where the vibrations of the rotor during run down vanishes.
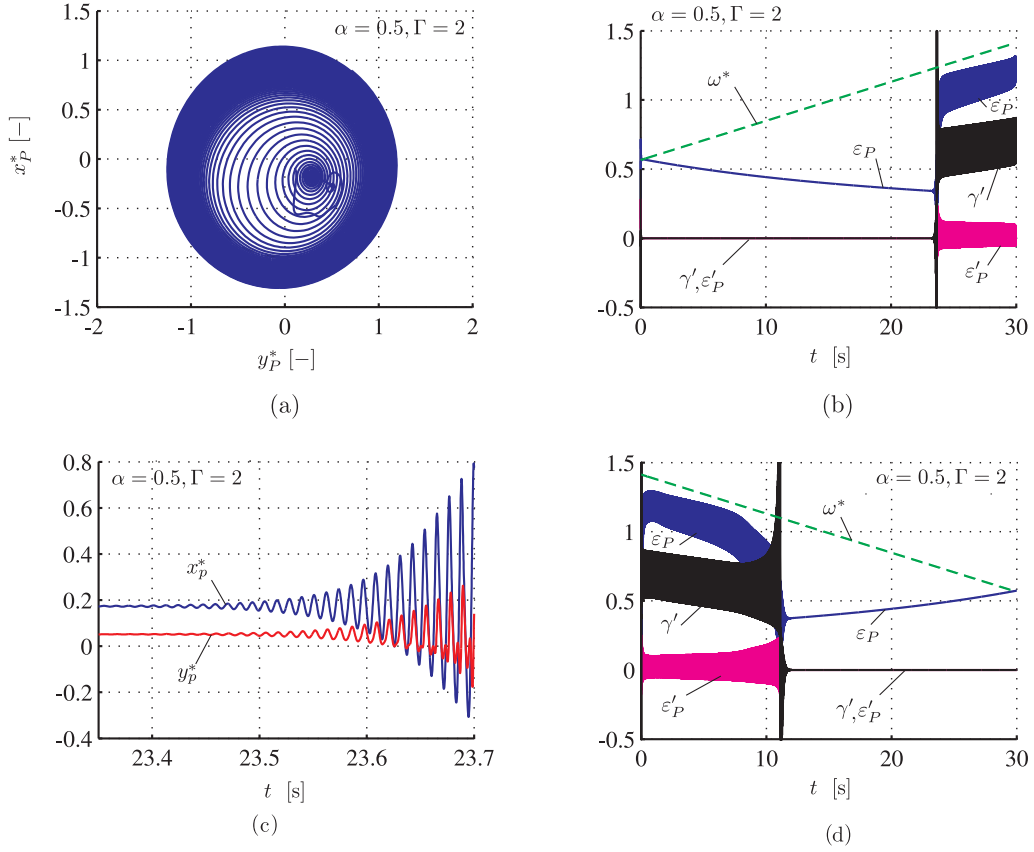
Figure 4: Trajectory of rotor center (a), state variables (b) and onset of self excited vibrations during run up (c), state variables during run down (d)

7.2 Steady-State-Stability

The steady state solutions $\boldsymbol{x}_0$ of (30) are determined by solving the algebraic equations

$$\boldsymbol{0} = \boldsymbol{X}(\boldsymbol{x}_0) \tag{31}$$

for $\boldsymbol{x}_0$. The stability of these steady state solutions $\boldsymbol{x}_0$ may be assessed by investigating the eigenvalues of the Jacobian $\boldsymbol{J} = \left.\frac{\partial \boldsymbol{X}}{\partial \boldsymbol{x}}\right|_{\boldsymbol{x}=\boldsymbol{x}_0}$. For a given angular velocity of the rotor, the stationary rotor position is asymptotically stable, if all real parts of the eigenvalues of $\boldsymbol{J}$ are negative. Derived from this condition, Figure 5 (a) shows the critical angular velocity of the rotor ω_s^*, where the transition between stable and unstable stationary journal position occurs. It might be observed that for an increasing parameter Γ (i.e. lower rotor mass) the stability threshold is shifted to lower rotor speeds. Furthermore, for the chosen set of parameters, an increasing compliancy α leads to a decrease of the threshold ($\Gamma = 2, 4$), while for a high rotor mass ($\Gamma = 0.5$) the threshold is shifted to higher rotor speeds. Initially, the results, in terms of the dependency on the bearing compliancy on the stability threshold are not as expected, compared with previous results, presented in [1]. Figure 5 (b) shows the stability threshold over a different, but comparable nondimensional compliance parameter α_W, which was obtained solely by another structure model, a Winklerfoundation or in terms of air bearings so-called simple elastic foundation model, see [8]. In both cases the same model reduction was conducted and the same parameter values were used. Summarizing, the physical difference between both models is the deformation of the structure in axial direction. In contrast to the results obtained by the here presented model, the transition between stable and unstable stationary solutions for stiff structures (low α) and light rotors is shifted to higher values, the softer the bearing housing is. But, comparing these effects with results found in literature, it turns out, that they are not inconsistent. For example LeLez et al concluded by presenting numerical results of one set of parameters based on a more elaborated bearing structure model in [11], that structural deformation, without energy dissipation, strongly enhances the bearing stability (steady state stability). Furthermore, Carpino and Talmage in [3] concluded, based on FE simulations,
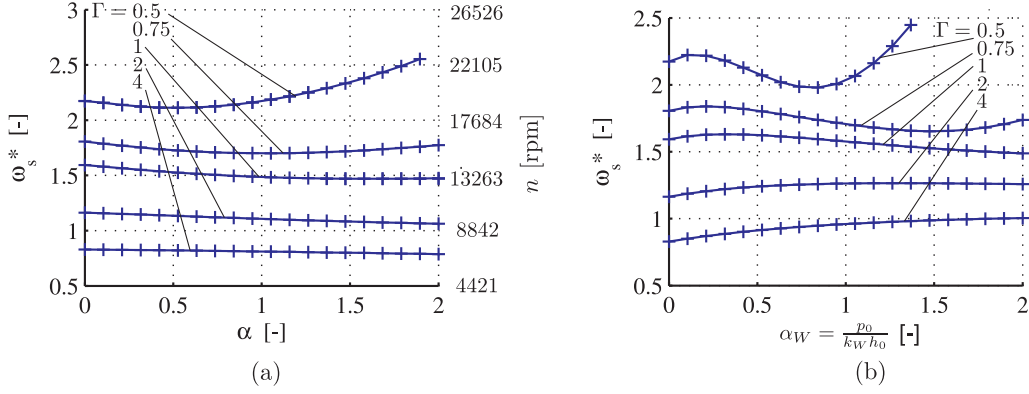
Figure 5: (a) Stability threshold over bearing compliance, (b) [1]

that an significant increase in bearing load capacity can be achieved by axially varying subfoil stiffness and that an optimal stiffness configuration exist. However, the stability of steady state solutions was not investigated, within this publication. Eventually, the error in both cases, caused by using the same shape functions, although having two different physical models is not yet comprehensively investigated.

7.3 Bifurcation Analysis

Using the nondimensional angular velocity ω^* as bifurcation parameter and studying the eigenvalues of $\boldsymbol{J}$ with increasing rotor speed, a non-hyperbolic stationary point with two conjugate complex imaginary parts (and vanishing real parts) occur at ω_s^*. Thus, an Andronov-Hopf-Bifurcation (H) can be identified, where a periodic solution

$$\boldsymbol{x}_{per}^{'} = \boldsymbol{X}(\boldsymbol{x}_{per}(\tau)) \tag{32}$$

bifurcates from a stationary solution, e.g. [14]. The period T is defined by the smallest non zero positive value, where the state vector $\boldsymbol{x}$ fulfills the condition

$$\boldsymbol{x}_{per}(\tau) = \boldsymbol{x}_{per}(\tau + T). \tag{33}$$

Within MatCont the boundary value problem (32) and (33) completed by the integral phase condition is solved by an orthogonal collocation method, [5], [10]. To determine the stability of the periodic solution the (complex) multipliers of the cycle, which are the eigenvalues of the monodromy matrix are investigated. In autonomous systems one multiplier has always an absolute value of 1. The remaining multipliers determine the stability of the cycle. If all remaining multipliers have magnitude less than one, the periodic solution is (asymptotically) stable. If one multiplier has a magnitude greater than one, the periodic solution is unstable.

Figure 6 (a) shows the stationary solutions and some limit cycles for the Cartesian coordinates x_P^* and y_P^* of the rotor's center P for a rigid bearing, as a function of the angular velocity ω^*. Figure 7 (a) shows the relating maximum eccentricity ε_P on the limit cycle or the stationary solution over the angular velocity. It is observable, that the stationary solutions (starting on the left side of the latter diagram) are tending towards the center, with increasing angular velocity, as already known form journal loci evaluations. Stationary solutions with angular velocities $\omega^* > \omega_s^*$, are unstable. At the Andronov-Hopf-Bifurcation H an unstable limit cycle is born, which further characterises the Andronov-Hopf-Bifurcation as subcritical. Following the unstable branch, at FB_1 a fold bifurcation of cycles, also known as limit point of cycles, emerges. Thus, the limit cycle becomes stable. Since the fold bifurcation FB_1 is located at a lower angular velocity than the Andronov-Hopf-Bifurcation H, an angular velocity interval exists, with two stable solutions - a stationary and a periodic. Within that interval and since no excitation exists, the initial state for a given angular velocity determines whether the system tends to the stationary or periodic solution. This characteristic explains the difference in the rotor speed of upcoming or decaying vibrations during run up and run down simulations. Within the investigated angular velocity interval no other bifurcation occurs, but beyond that interval the topology of solutions changes.

Paper-ID 52
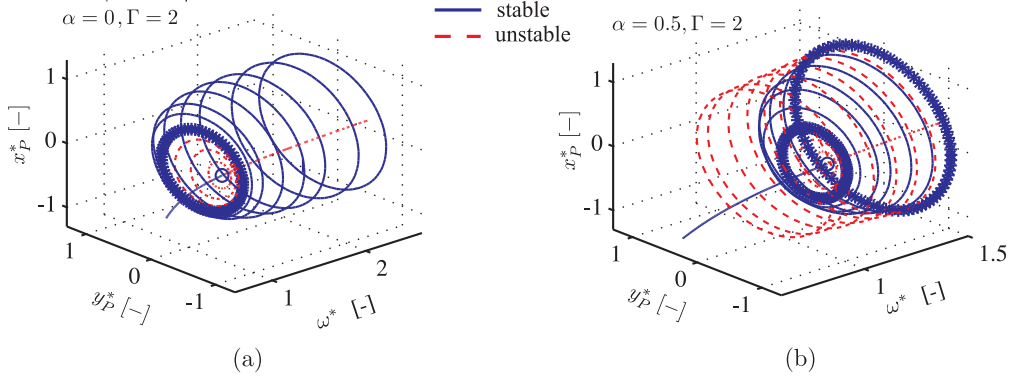
Figure 6: Stationary solutions and limit cycles - rigid bearing (a), compliant bearing (b)
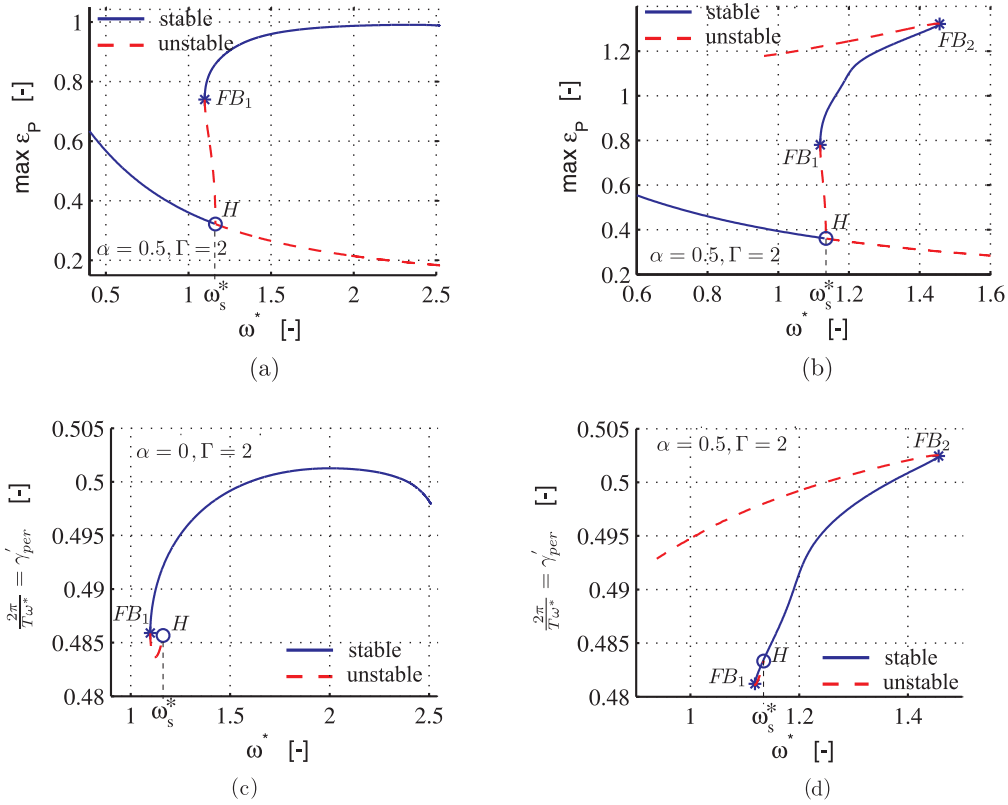
Figure 7: Maximum eccentricity and whirl speed - rigid bearings (a), (c), and compliant bearings (b), (d)

For autonomous systems, the period T of periodic solutions, relating to different angular velocities, is generally neither known, nor constant. Figure 6 (b) shows γ'_{per}, which can be interpreted as the averaged angular velocity of the whirl motion of the rotor's center, over the angular velocity of the rotating journal ω^*. One might observe, that the averaged angular velocity is roughly half the rotor's angular velocity $\gamma'_{per} \approx \frac{\omega^*}{2}$, which could already been established from Figure 4 (b), (d). Based on the similar and well known behavior of rotors in oil-lubricated fluid film bearings, the presented characteristics of self excitation with approximately half rotor speed could be called air-whirl.

When compliancy of the bearing housing ($\alpha \neq 0$) is taken into account, some qualitative changes appear, see Figure 6 (b) and Figure 7 (b), (d). A different angular velocity of the rotor, where the Andronov-Hopf-Bifurcation (H) is located could already be investigated by the steady state stability analysis. Higher amplitudes of the whirl motion, due to the deformations of the bearing, where observed during run up or run down simulations. But the secondary fold bifurcation FB_2 doesn't exist for rigid bearings within the investigated angular velocity interval.

Again, at FB_2 two limit cycles, one stable and one unstable collide and disappear. Thus, for angular velocities higher than the second fold bifurcation no stable solution exists, which could also be verified by time integration. From Figure 7 (d) it could be concluded that the compliancy seems to have a minor influence on the averaged angular velocity of the rotor's whirl motion γ'_{per}, which remains approximately at half rotor speed.

8 Summary

To identify the influence of the compliancy of air foil bearings on the rotor's behavior, the simplest rigid rotor model is coupled with a simple bearing model and solved simultaneously. The overall model is transformed in non-dimensional form and the number of independent variables within the fluid equation is reduced by using a Galerkin approach of Kantorovich type, aiming for a time efficient model. The derivatives w.r.t. the remaining spatial circumferential coordinate are discretised by finite central differences and the overall model is written as an autonomous first order system of coupled nonlinear ordinary differential equations. The stability threshold ω^*_s for the stationary journal position (steady state solution) is investigated by varying the nondimensional compliance parameter and the nondimensional parameter of the rotor mass. It is numerically shown, that the onset of whirl motion is shifted to higher rotor speeds, the heavier the rotor is, but no general rule for the influence of the compliancy on the stability threshold could be deduced. A comparison with results found in literature, showed the sensitivity of the structure stiffness modelling on the rotor's behavior. Besides steady state solutions, stable and unstable periodic solutions exist. Stable periodic solutions represent the air whirl phenomena, with approximately the half rotor's angular velocity, independent the compliancy of the bearing. If a bearing compliancy is considered, the rotor whirls with higher radii and furthermore another angular velocity threshold could be identified. Beyond no stable solution exists.

Future work is addressed to more elaborate bearing models, in particular to modelling the structure stiffness and to the validation of the fluid equation reduction. In further steps, more physical properties, like damping and friction within the bearing structure should be included. Additionally, the investigated rotor models will become more complex.

REFERENCES

[1] Baum, C., Hetzler, H., Seemann, W. (2014): On the dynamics of a rigid rotor with static unbalance symmterically mounted in compliant air bearings. *Proc. of IFToMM ICORD 2014*, Milan

[2] Bonello, P., Pham, H. M. (2014): The efficient computation of the nonlinear dynamic response of a foil-air bearing rotor system. *JSV*, **333**, p. 3459 - 3478

[3] Carpino, M., Talmage, G.(2008): Subfoil stiffness effects in gas-lubricated foil journal bearings. *Trib. Trans.*, **51**, p. 602 - 608

[4] DellaCorte, C. (2012): Oil-Free shaft support system rotordynamics: Past, present and future challenges and opportunities. *MSaSP*, **29**, p. 67 - 76

[5] Govaerts, W., Kuznetsov, Y. A., De Witte, V., Dhooge, A., Meijer, H.G.E., Mestrom, W., Riet, A.M., Sautois, B. (2011): *MATCONT and CL MATCONT: Continuation toolboxes in matlab*, Gent and Utrech University

[6] Gross, W. A. (1969): SA review of developments in externally pressurized gas bearing technology since 1959. *Journal of Lubrication Technology*, 91, 161-165 (1969)

[7] Gross, W. A., Matsch, L. A., Castelli, V., Eshel, A. Vohr, J.H., Wildmann, M. (1980): *Fluid film lubrication*. John Wiley and Sons, Inc.

[8] Heshmat, H., Walowit, J.A., Pinkus, O. (1983): Analysis of gas-lubricated foil journal bearings. *ATJLT*, **105**, p. 647

[9] Kantorovich, L. V., Krylov, V. I., Benster, C. D. (1964): Approximate methods of higher analysis, Interscience

[10] Kuznetsov Y. A. (1998): *Elements of applied bifurcation theory*. Springer, A.M.S. Vol 112

[11] Le Lez, S., Arghir, M., Frene, J. (2009): Nonlinear numerical prediction of gas foil bearing stability and unbalance response. *J Eng Gas Turb Power*, **131**

[12] San Andrés, L. and Kim, T. H. (2009): Analysis of gas foil bearings integrating FE top foil models *Tribology International*, **42**(1), pp. 111–120.

[13] Szeri, A. Z. (2011): *Fluid film lubrication*. Cambridge University Press, 2nd ed

[14] Wiggins, S. (2003): *Introduction to applied nonlinear dynamical systems and chaos*. Springer, 2nd ed